JATIS Journal of Astronomical Telescopes, Instruments, and Systems

RESEARCH PAPER

Mexico-UK Submillimeter Camera for AsTronomy focal plane performance at the Large Millimeter Telescope

Marcial Becerril Tapia,[a,b,*] Peter A. R. Ade,[a] Emmaly Aguilar Pérez,[b] Peter S. Barry,[a] Thomas L. R. Brien,[a] Edgar Castillo-Domínguez,[c] Christopher Dodd,[a] Christopher Dunscombe,[a] Stephen Eales,[a] Daniel Ferrusca,[b] Víctor Gómez-Rivera,[d] Peter Hargrave,[a] José Luis Hérnandez-Rebollar,[b] Amber Hornsby,[e] Julian House,[a] David Hughes,[b] Abraham Luna,[b] José Miguel Jáuregui-García,[b] Philip Mauskopf,[f] Dulce Murias,[g] Andreas Papageorgiou,[a] Enzo Pascale,[h] Nicolas Peretto,[a] Abel Pérez,[b] Samuel Rowe,[a] Iván Rodríguez,[b] David Sánchez-Argüelles,[b] Matthew W. L. Smith,[a] Kamal Souccar,[i] Rashmikant Sudiwala,[a] Ana Torres-Campos,[b] Carole Tucker,[a] Miguel Velázquez,[b] Salvador Ventura-González,[j] Ian Walker,[a] and Simon Doyle[a]

[a]Cardiff University, School of Physics and Astronomy, Cardiff, United Kingdom
[b]Instituto Nacional de Astrofísica, Óptica y Electrónica, Puebla, Mexico
[c]University of Oxford, Physics Department, Oxford, United Kingdom
[d]Corporación Mexicana de Investigación en Materiales S. A. de C. V., Saltillo, Mexico
[e]University of California, Berkeley, Berkeley, California, United States
[f]Arizona State University, Tempe, Arizona, United States
[g]Centro de Investigaciones en Óptica A.C., León, Mexico
[h]La Sapienza Universitá di Roma, Dipartimiento di Fisica, Roma, Italy
[i]University of Massachusetts, Department of Astronomy, Amherst, Massachusetts, United States
[j]Université Paris-Saclay, IRFU, CEA, Gif-sur-Yvette, France

ABSTRACT. The Mexico-UK Submillimeter Camera for AsTronomy (MUSCAT) is a continuum camera in the 1.1-mm band for the Large Millimeter Telescope (LMT), with 1458 lumped-element kinetic inductance detectors distributed across six arrays. Installed on the telescope at the end of 2021, we present the characterization of the detector beams of four of the six arrays based on the beam map observations of bright point sources developed during the first commissioning campaign between February and June 2022. With all the observations, we estimate the average positions of each detector with an average error in azimuth of less than 0.70 arcsec and less than 1.05 arcsec in elevation. From the positions, we created the coadded maps of all the detectors, from which we selected only eight observations to calculate the mean beam width of MUSCAT-LMT, of 6.32 ± 0.36 arcsec $\times 5.78 \pm 0.19$ arcsec. By stacking the maps, we identify the sidelobes with three main structures whose amplitudes are ~3% with respect to the main beam.

Keywords: millimeter camera; kinetic inductance detectors; focal plane characterization; beam optimization; commissioning observations

Paper 24066G received May 12, 2024; revised Sep. 4, 2024; accepted Sep. 11, 2024; published Oct. 25, 2024.

*Address all correspondence to Marcial Becerril Tapia, mbecerrilt92@gmail.com

1 Introduction

Infrared/millimeter radiation represents ∼50% of all the energy in the extragalactic background light. The optical/near-infrared radiation emitted by all the stars via nucleosynthesis throughout cosmic history is absorbed and re-emitted by dust in the wavelength range from 3.5 to 1000 μm.[1] The detection of this millimeter/submillimeter radiation plays a key role in exploring colder, denser, and darker regions, such as the early stages of star formation within molecular clouds, protoplanetary disks, and high-redshift dusty starburst galaxies.

In this sense, the last decades have witnessed important technological advances on several fronts in the millimetric universe exploration, from larger telescopes with wider fields of views to the increasing amount of detectors with higher sensitivities on the focal plane[2,3] managed by more robust readout systems with higher multiplexing capacities.[4]

Leading facilities such as balloon-borne telescopes such as Balloon-Borne Large Aperture Submillimeter Telescope–The Next Generation (BLAST-TNG),[5] space missions such as the Herschel Space Observatory,[6] and interferometers such as the Submillimeter Array (SMA) in Hawaii, or the Atacama Large Millimeter/submillimeter Array in Chile.

Considering ground-based single-dish telescopes, we find the 15-m James Clerk Maxwell Telescope in Hawaii, with successful cameras such as Submillimeter Common-User Bolometer Array (SCUBA),[7] based on semiconductor bolometers, that performed the first deep field maps detecting a significant population of high-z galaxies;[8,9] followed by SCUBA-2,[10] based on transition-edge sensor (TES) detectors, with a mapping speed up to 100 times greater than its predecessor. Recently, new cameras are adapting the novel Kinetic Inductance Detectors (KIDs),[2] such as Néel IRAM KID Array (NIKA)[11] and its successor NIKA-2[12] on the IRAM 30-m telescope in Spain, due to its high scalability performance.

The Large Millimeter Telescope (LMT),[13] a 50-m diameter single-dish radio-telescope located at the summit of the Sierra Negra volcano, at an altitude of 4600 m, in Mexico, housed the 144-pixel bolometer-based camera AzTEC,[14] followed by a second generation of KID-based continuum cameras (>1000 pixels), TolTEC[15] and the Mexico-UK Submillimeter Camera for AsTronomy (MUSCAT).

MUSCAT is a large-format continuum camera in the 1.1-mm band[16,17] installed in late 2021 in the LMT. Its focal plane brings together 1458 aluminum lumped-element KID,[18,19] distributed across six sub-arrays of 243 detectors each read through frequency domain multiplexing,[20–22] operating continuously at ∼120 mK.[17,23,24] Exploiting the LMT's high sensitivity, MUSCAT will perform deep area surveys in reasonable integration times and an unprecedentedly high angular resolution (∼5 arcsec in the diffraction limit).

MUSCAT's commissioning, characterization, repair, and upgrade tasks have been divided into two runs. Run 1 saw the camera installation in the receiver cabin, with the first light from engineering and astronomy on the LMT, as well as the first commissioning observations campaign from February to June 2022. In run 2, we implemented repairs to the radio frequency (RF) lines, and then, we developed the second commissioning campaign, starting the observations of the scientific proposals. Regrettably, the outbreak of diverse natural disasters near the LMT led to prematurely canceling the 2023 observation season.

In this paper, we present the detector characterization results of the MUSCAT arrays available during the first commissioning campaign at the telescope, i.e., based on run 1 observations. In Sec. 2, we briefly describe the main characteristics of the instrument and its operation in the LMT. Section 3 summarizes the observations made during run 1 and describes the MUSCAT-LMT beam optimization procedure and the data reduction process. In Sec. 4, we present the main results based on the beam map observations selected and grouped by sub-array, such as the detectors' positions, beam widths, and array yields, as well as the instrument's beam shape and the sidelobes found in the stacked map of all the observations. Finally, in Sec. 5, we present the conclusions derived from this work.

2 MUSCAT Operation on the LMT

MUSCAT detects millimeter radiation through the synergy of four main subsystems: detectors, cryogenics, cold optics and filtering, and readout. The diagram in Fig. 1 presents an overview of their location, functions, and interconnections in the instrument.

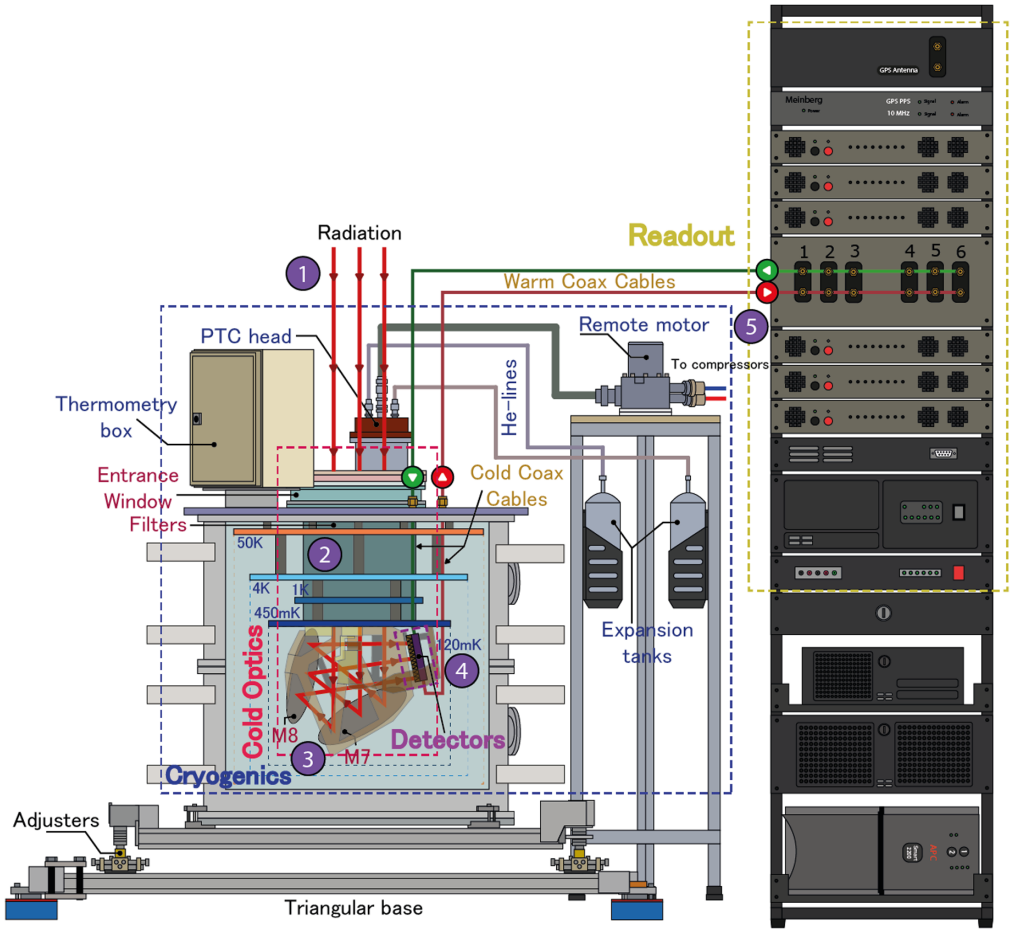

Fig. 1 MUSCAT operation diagram. The radiation entering through the receiver window vertically (1) passes through a series of metal-mesh low-pass filters to the central part of the instrument (2), where a pair of mirrors (M7 and M8) in a crossed Dragone configuration (3) reflects it to the focal plane to be absorbed by the detector arrays (4). Next, a pair of transmission lines carrying probe tones record the intensity of the incident radiation and carry it out of the camera to the readout subsystem for decoding using frequency multiplexing (5). One of the most significant advantages of KID-based instruments is that the vast majority of the readout electronics have been moved outside to room temperature, which is easier to handle. The operation of the detectors is only achieved at sub-Kelvin temperatures within a cryostat that manages to cool them down to ~120 mK, through successive thermal stages, 50, 4, 1, and 0.45 K. The dashed boxes indicate the four subsystems that compose the camera: detectors, cold optics and filtering, cryogenics, and readout.

The cold optics and filtering direct the light beam collected by the telescope to the detector arrays in the focal plane and define the instrument's bandwidth. The detectors, superconducting resonators, absorb the photons of the incident millimeter radiation, causing its resonance frequency shift, which the readout subsystem measures through frequency multiplexing, digitizing, and storing the data for further processing and analysis.

Following the path of light, illustrated in Fig. 1, the radiation enters the camera through the receiver window, a 33.5-cm diameter disc of ultra-high molecular weight polyethylene, thin to minimize dielectric losses but robust enough to maintain the high vacuum of the cryogenic chamber ($<1 \times 10^{-6}$ mbar). Inside the instrument, the radiation passes through a series of metal-mesh filters placed in several of the cryostat's cooling stages. These filters reject optical and near-infrared (NIR) radiation from outside and shield against the interior infrared radiation emitted by the 300, 50, and 4 K cryogenic stages, allowing the operation of the cryostat at sub-Kelvin temperatures. In-band light is focused onto the instrument's focal plane through the M7/M8 aluminum mirrors in crossed Dragone configuration.[25,26]

In the focal plane, the radiation is coupled to each of the detectors in the array through feedhorns, which also reject long wavelengths. Thus, the filters arranged along the internal optical path of the instrument (low-pass filters), together with the feedhorns (high-pass filters), define the instrument's bandwidth, ~50 GHz, centered at 275 GHz (1.1 mm).[27]

The detectors are superconducting inductor-capacitor (LC) resonators with fixed capacitance and variable inductance depending on the incident radiation. Each detector has a unique resonance frequency achieved by a well-defined capacitance. The absorption of millimeter radiation causes the splitting of Cooper pairs in the superconducting inductive section, which in turn produces an increase in the inductance of the resonator, leading to a change in the circuit's resonance frequency. For each of the six arrays of detectors, there is a readout channel that injects probe tones through a single transmission line, corresponding to each detector's resonant frequency. The detector's resonance shift modulates the probe tone through which the incident radiation is derived.

Due to the fabrication, the six detector arrays are divided into three pairs, or MUSCAT Developments (MD), sharing the same deposition silicon wafer, packaging box, and hornblocks.[27] According to the manufacturing order, arrays 1 and 2 belong to MD-M, 3 and 4 to MD-J, and 5 and 6 to MD-F.

The cryostat is cooled in five successive thermal stages: 50 and 4 K through a pulse tube cooler (PTC), 1 K and 450 mK by two anti-phase continuous sorption fridges,[28] and finally, a miniature dilution fridge achieves the 120 mK stage,[23,24] where the detectors are mounted. The functions of the intermediate stages range from providing operating temperatures for other equipment, such as low-noise amplifiers, to thermal isolation points for colder stages.

In Fig. 2, we present the general operation diagram of the MUSCAT-LMT system. The radiation collected by the 50-m-diameter primary reflector (M1) is reflected to a second hyperbolic mirror (M2), which leads it into the receiver cabin through the telescope apex. There, a series of warm mirrors, M3, M4, M5, and M6, the last two in crossed Dragone configuration, directs the radiation into the interior of the MUSCAT camera.

A water/glycol system cools the MUSCAT compressor. It comprises two circuits: one that continuously extracts heat from the compressor and heats the water/glycol mixture in the tank and another that periodically cools the water/glycol in the tank by circulating the liquid through a chiller.

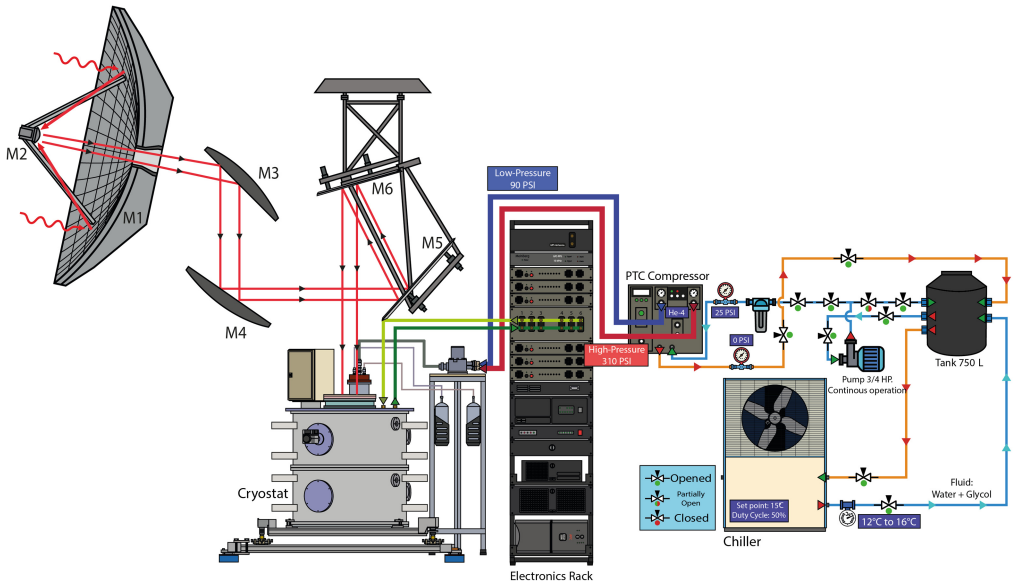

Fig. 2 General operation diagram of MUSCAT at the LMT. The radiation collected by the 50-m dish is reflected through M2, M3, M4, M5, and M6 mirrors to the MUSCAT window. The millimeter radiation is absorbed by its detectors and measured through the readout subsystem in the electronics rack. The heat extracted from the MUSCAT cryogenic subsystem is conducted to a Helium compressor, where the water/glycol cooling system extracts it and finally dissipates it to the environment.

Due to RF line failures in two channels during run 1 observations, breakage in coaxial cables, wire bonding, and a malfunction of one of the low-noise amplifiers, this paper only reports the results of arrays 2, 3, 5, and 6, which were read out through RF channels named "clones," "sith," "empire," and "jedi," respectively.

3 Methods

3.1 Observations

From February to June 2022, we developed the MUSCAT-LMT first commissioning campaign, performing observations at different elevations under different atmospheric conditions. In particular, for the characterization of the readable detectors, we observed bright point-like sources (we selected the brightest sources in the 1-mm band from the list of submillimeter calibrators of the SMA,[29] available in the LMT sky during the observation), in a field large enough for all the detectors in the focal plane, with a circular field of view of 240 arcsec diameter, to pass through the source. These observations, better known as beam maps, consist of large 500 arcsec × 500 arcsec azimuth raster scans with a telescope scan rate of 100 arcsec/s and an elevation step that ranges from 2 to 3 arcsec.

For run 1, we made 14 beam map observations of the sources 3C279, a blazar with a very active nucleus and a prominent radio jet,[30] and Neptune. Table 1 summarizes the main characteristics of these observations, including the mean elevation and mean atmospheric opacity at 225 GHz recorded by the LMT radiometer.

3.2 Initial Setup

The MUSCAT-LMT system optimization precedes each beam map observation through a set of tasks to maximize the detectors' response and correct the antenna's pointing, focal length, and

Table 1 Run 1 beam map observations. For each observation, we present the observation number and date, source name, average elevation, and opacity recorded at 225 GHz by the LMT radiometer.

ObsNum	Date	Source	Mean opacity at 225 (GHz)	Mean elevation (deg)
094468	25/02/2022	3C279	NA	55.19
094469	25/02/2022	3C279	NA	50.98
094471	25/02/2022	3C279	NA	45.71
098811	28/04/2022	3C279	0.33	64.82
099077	05/05/2022	3C279	0.09	61.81
099087	05/05/2022	3C279	0.09	37.86
099108	05/05/2022	3C279	0.08	21.40
100280	26/05/2022	3C279	0.22	62.32
100286	26/05/2022	3C279	0.19	54.88
100292	26/05/2022	3C279	0.22	45.33
100781	07/06/2022	Neptune	0.14	42.00
100785	07/06/2022	Neptune	0.13	50.84
100789	07/06/2022	Neptune	0.12	58.03
100908	08/06/2022	Neptune	0.15	34.30

For the observations of February 25, 2022, the radiometer was not available (NA).

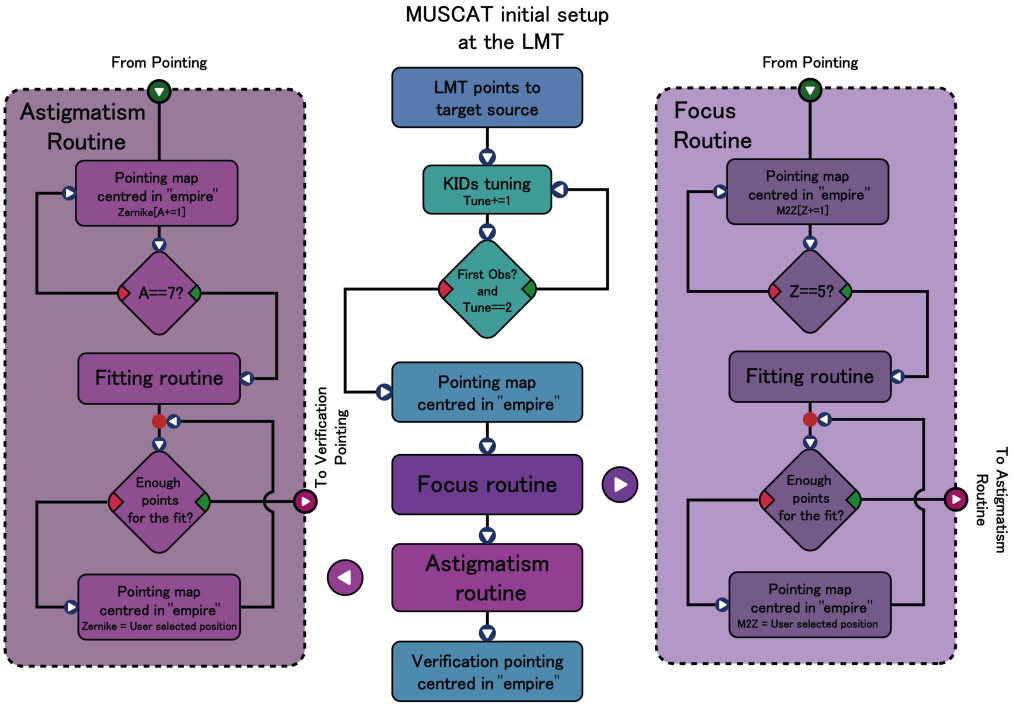

Fig. 3 Flowchart of the MUSCAT initial setup at the LMT. Once the telescope points to a bright point source, we perform the tuning procedure twice if this is the first observation of the night and once in any other case. Then, we carry out a pointing observation to check the initial beam status. Next, we correct the system's focal length through the focus routine (right), where we measure the source amplitude for five different offset positions of the M2 mirror. We then similarly correct the astigmatism of the primary reflector using the astigmatism routine (left), where we measure the source amplitude for a Zernike coefficient sweep of the antenna. The correction parameters are the M2's Z-axis offset and the M1's Zernike coefficient, which maximizes the source's amplitude. Finally, to verify the final state of the beam, we perform one last pointing observation.

surface, known as the initial setup. It is also carried out at the beginning of the night and repeated every time the beam presents significant broadening or distortions due to thermal contractions in the antenna caused by the variation in the site weather conditions throughout the night. The flowchart in Fig. 3 illustrates the initial setup process, which consists of the detectors' tuning, intrinsic to the KID operation, and the routine beam optimization procedure at the LMT: focus and astigmatism tasks and verification pointing maps.

3.2.1 *Detectors tuning*

The tuning procedure updates the probe tone frequencies to the current detector's resonance frequencies, compensating for any displacement caused by the background loading variation due to the atmosphere's local conditions in the line of sight of the source, which depends on the airmass (elevation) and the opacity. It is carried out in four steps: (i) we perform a transmission frequency sweep for all the detectors in a narrow window, ~100 kHz; (ii) we calculate the new resonance frequency of each detector, selecting the point at which the complex transmission varies fastest with respect to the sweep frequency, where the detector response is maximum; (iii) then, we upload these resonance frequencies to the readout subsystem;[20,22] and (iv) we perform a detector's frequency sweep, similar as step (i), to verify that the tones match the resonance frequencies. Rowe et al.[22] describe the MUSCAT tuning procedure in greater detail.

We perform the tuning procedure twice at the beginning of the night (due to the significant load change from dark to sky temperature), when we observe a new source, or it has been continuously observed for more than an hour, where a significant change in elevation due to prolonged tracking have impacted the background load on the detectors.

3.2.2 *Beam optimization*

Following the detector tuning, we perform the MUSCAT-LMT beam optimization. Illustrated in Fig. 4, it consists of the next steps:

1. Initial pointing map to inspect the beam status: It comprises a 50 arcsec × 50 arcsec azimuth raster scan map centered on array 5, with an elevation step of 5 arcsec and a scanning speed of 50 arcsec/s, having an exposure time of ∼1 min.

   If the beam is wider or distorted, or the secondary lobes are prominent, we continue the focus routine; otherwise, we perform the beam map observation directly. The top map of Fig. 4 shows the preliminary appearance of the beam in a typical observation: strongly dilated and deformed.

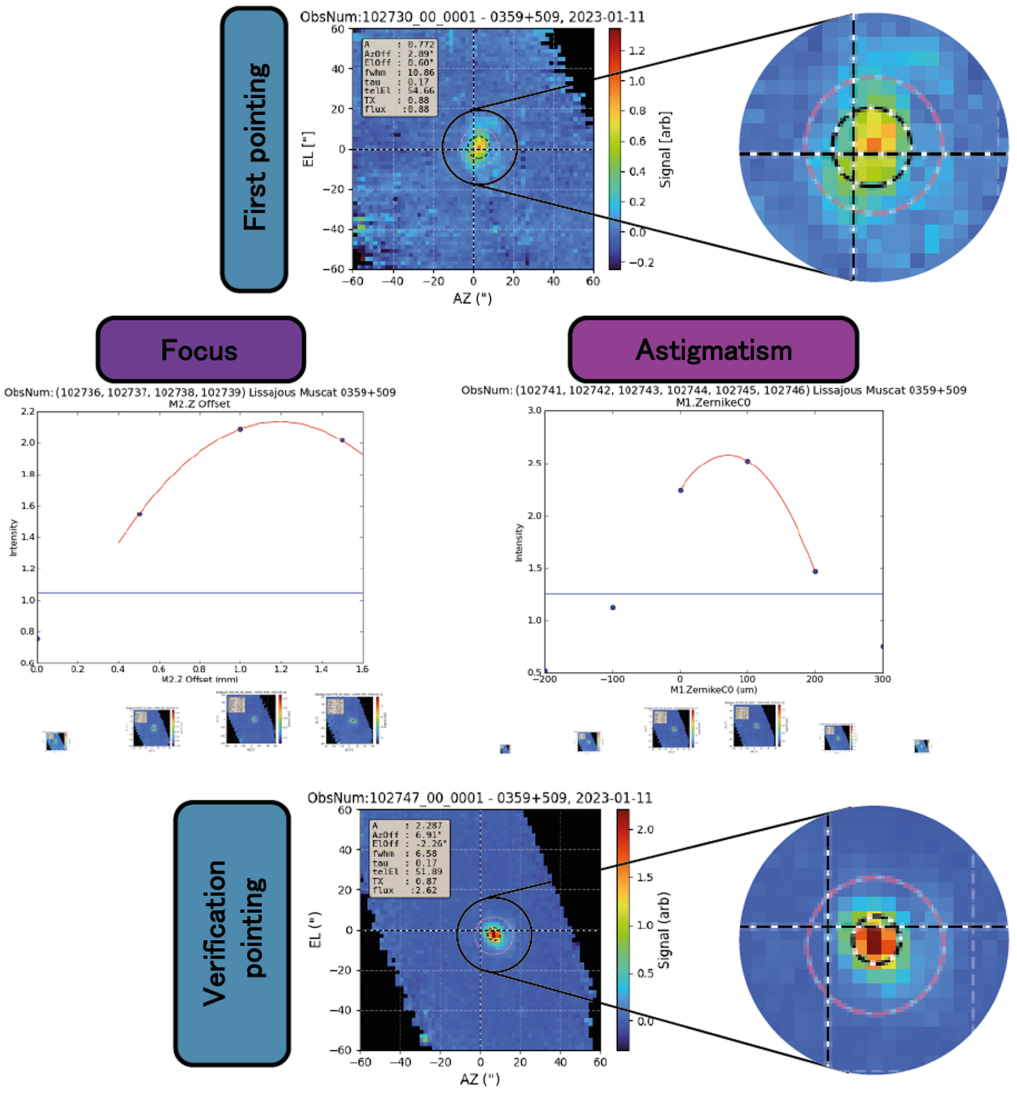

Fig. 4 Initial setup for MUSCAT-LMT observations. The first pointing map (top) evaluates the status of the beam; in this case, it is far from ideal: wide and with prominent secondary lobes. The correction involves a focus routine, which adjusts the *M*2 mirror offset in the *Z*-axis to maximize the source amplitude. Next, we apply the astigmatism correction, where the Zernike coefficients of the primary mirror are adjusted to maximize the source amplitude. Finally, we perform one last pointing observation to verify the resulting beam (bottom). Here, we see how the quality of the beam has improved substantially; the width, ∼6 arcsec, is close to the diffraction limit, the secondary lobes have faded, and the amplitude is approximately three times greater than the initial pointing. Focus and astigmatism chart credits: LMT project.

2. Focus routine: Due to thermal deformations in the primary mirror, refocusing the telescope beam on the MUSCAT focal plane is constantly necessary, moving the M2 mirror along the Z-axis (toward/away from the M1 mirror).

   It consists of five pointing observations sweeping the offset position of the M2 mirror along the Z-axis, from -2 to 2 mm in steps of 1 mm. For each map, we obtain the source amplitude using a Gaussian fit. We plot these amplitudes as a function of the offset and then fit a second-order polynomial only to those points whose values are greater than half of the maximum amplitude. The offset corresponding to the curve's maximum constitutes the final value added to the M2's Z position.

3. Astigmatism routine: It corrects the surface of the LMT's primary reflector, adjusting the Zernike coefficients that maximize the antenna gain.

   It is implemented through seven pointing observations in which the Zernike coefficients of the primary reflector vary from -300 to 300 μm in steps of 100 μm. Similar to the focus routine, we estimate the source amplitude on each map, plot them as a function of the Zernike coefficient, fit a second-order polynomial to points greater than half the maximum amplitude, and estimate the Zernike coefficient corresponding to the maximum amplitude of the fit.

4. Verification pointing: Finally, we perform a final pointing observation to inspect the status of the resulting beam. The bottom graph of Fig. 4 presents the beam optimization result of the initial setup. It shows a clear improvement in contrast to the first pointing observation: the amplitude is three times greater, the width two times smaller, and the sidelobes are noticeably diminished.

3.3 Data Reduction

The observations are processed through MUSpipe,[31] a pipeline tool programmed in Python3 and designed for MUSCAT observation reductions. As shown in the flowchart of Fig. 5, it carries out the reduction in three stages: (i) pre-processing, for the initial preparation of the timestreams;

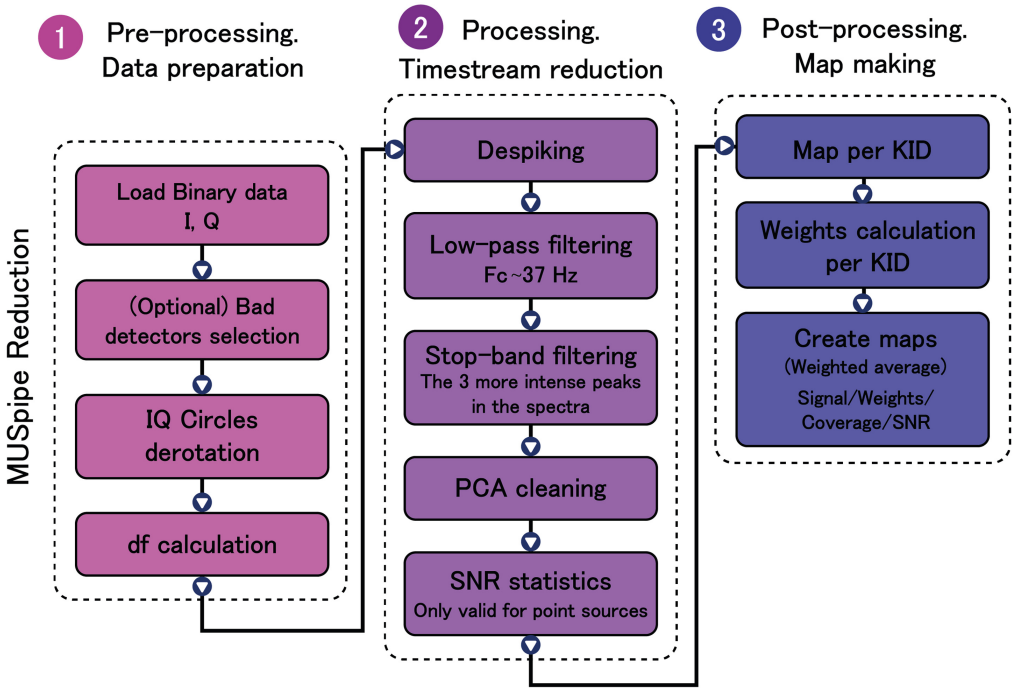

Fig. 5 Flowchart of the MUSpipe reduction process. It consists of three stages: (1) pre-processing, where we load the I/Q timestreams, identify and discard the "bad" detectors, correct the baseline effect (derotation), and estimate the resonance frequency shift; (2) processing, where we eliminate cosmic rays, glitches, apply filters, and remove the atmosphere; and (3) post-processing, where we make the maps by applying inverse-variance weighting.

(ii) processing, for the timestreams cleaning; and (iii) post-processing, where it makes the maps combining instrument timestream with the telescope pointing data.

3.3.1 *Pre-processing*

For each observation, MUSCAT records the temporal response of the I/Q quadrature readout signals modulated by the kinetic inductance changes in the detectors produced by the absorption of millimeter radiation from the sky. These I and Q timestreams are sampled at 488.28 Hz. In addition, the system records the complex transmission frequency sweeps for all the detectors from the tuning associated with a particular observation.

During pre-processing, we first identify and discard damaged or spurious detectors to avoid contamination during timestream cleaning and map generation. We consider that a detector is "bad" if it meets any of the following criteria:

- Frequency collision: If the frequency distance between two resonators is less than 25 kHz. When two resonators are very close to each other in the frequency domain, their responses interfere, producing false detections.
- Weak correlation connections: We say that there is a connection between two detectors if the association measure (AM) of the I/Q magnitude of their timestreams is greater than 0.75. The detectors with less than 10 connections are labeled as "bad."

The AM between two timestreams, defined by Ildar et al.,[32] is the association function (AF) average between two sliding windows. The AF indicates the degree of similarity between two time series on a scale defined by the size of the sliding window. This ranges from -1 to 1. It is 1 when the time series are identical, 0 when they have no relation, and -1 when anti-correlated. The value of AF changes depending on the window size; two time series may have little relation on small scales, but this could be very high on large time scales.

For each observation, we obtain the magnitude of the I/Q timestreams per detector and calculate the AM by averaging the AF among sliding windows from 7400 to 7500 samples among all possible combinations of detectors.

This window size is equivalent to correlation analysis on time scales of $\sim$15 s, large enough to visualize large-scale variations due to the atmosphere and the telescope's motion (elevation change), avoiding the random variations intrinsic to the instrumental noise on short scales.

Assuming all detectors observe the same section of the sky [each pixel observes a different region of the sky. Still, as the distance between them is small (a few arcseconds) with respect to the atmosphere fluctuations scale, we can presume that the atmosphere that they all observe has the same properties], the selected window is sensitive to changes due to the atmosphere, and ideally, the AM should be very high among all the detectors. We have observed that in those cases where the AM of a detector with the rest is below 0.75 on less than 10 times, the detectors are overdriven, and their timestreams present numerous glitches; they have low-quality factors (likely to be a fake detector as a feature on the baseline) or are excessively noisy.

Then, we correct the quadrature signals phase by undesired effects on the transmission line, such as the cable delay, standing waves, or residual mismatches. From the transmission frequency sweep made during the tuning, we calculate per detector (i) the center of the I/Q circle in the complex plane and (ii) the angle between the line that joints the I/Q circle center to the resonance frequency point and the I-axis. Next, we correct (derotate) the I/Q frequency sweep and the I/Q timestreams by applying the translation and rotation matrices, the opposite distance, and angle calculated above.

From the derotated frequency sweeps, we calculate the phase as a function of frequency $\phi(f) = \arctan(I(f)/Q(f))$. In the vicinity of the resonance, the phase and frequency follow a linear relation, so given a quadrature signal in the time domain from the timestream, we can estimate the phase and then the resonance frequency shift by linear interpolation.

3.3.2 *Processing*

The detectors' resonance frequency shift timestreams are cleaned by applying a series of filters to suppress glitches and cosmic rays (despiking), eliminating noise signals whose frequencies are well-defined, purging high frequencies, and extracting atmospheric components.

The despiking routine removes intense short-duration events, such as the impact of cosmic rays, electrical glitches, or sudden telescope movements. The algorithm derives the timestream with respect to time and selects those points above a threshold, typically 4σ. Next, it extracts regions from the timestream centered on these points with a user-defined size, typically 150 samples, and calculates the mean value, μ_r, and standard deviation, σ_r, at the edges of the region. If the number of points above 4σ is less than certain continuous points, commonly 4 points (with the typical scan rate of 100 arcsec/s and the MUSCAT sampling rate of 488 Hz, the expected width of a 5-arcsec point source is 27 samples, any narrower event is potentially due to cosmic rays or electronic glitches), is considered a spike. Then, it is replaced by random values generated following a normal distribution with the mean μ_r and standard deviation σ_r. Otherwise, the event is preserved.

In most beam map observations, the spectra present multiple well-defined, intense, narrow spikes. Some have been related to mechanical vibrations in the receiver room from the helium compressors and the PTC that has been transmitted to the MUSCAT mirrors, and its harmonics; however, in most, the origin is unclear. We apply a sinc-type low-pass filter to all timestreams with a cutoff frequency of 36 Hz, from where most of the spikes are presented, as well as notch-type band-stop filters with quality factors equal to 10 for the three most intense peaks below this cutoff frequency.

The last cleaning process involves atmospheric subtraction, the dominant radiation component in the MUSCAT band at the LMT. We expect the timestreams of most detectors to have similar shapes (in the matrix of AMs among the detectors of Sec. 3.3, the high level of correlation among the detectors on scales of atmospheric variation is also revealed), differing from each other only by the time the source passes through a particular detector and its intrinsic noise. MUSpipe employs the principal components analysis (PCA) (using the scikit-learn package for Python3) to obtain the common components among the selected detectors, mostly the atmosphere's contribution, and subtract them, preserving the source. We will refer to these resulting signals as the cleaned timestreams.

As demonstrated in Tapia et al.,[27] the detectors of the arrays that share the same deposition wafer and the same manufacturing process have similar characteristics: resonance frequencies, responsivities, and noise levels; hence, we get the principal components only among detectors of the same array.

We have seen that an over-substraction region around the source is formed as we extract components. From a certain point on, as we remove more components, we no longer reduce the timestream noise but also begin to extract the source itself. To determine the number of components to remove, we calculate the quantity that maximizes, per detector, the signal-to-noise ratio (SNR) of the source in the timestream. We calculate the first 40 common components for all detectors and extract them one by one while calculating, in each case, the SNR of the source in the timestream of each detector. In this way, for each detector, there is a relation between the number of removed components and the SNR, to which we fit a second-order polynomial. Then, the number of components to remove for a given detector is where the fit reaches the maximum SNR (because the source amplitude in the timestream is calculated from a Gaussian fit, this procedure only applies to point-source observations, as the beam maps). Nevertheless, the number of components to subtract remains an open topic because other little explored factors also influence, such as the time chunk size (in all the reductions that we present in this paper, we use a time chunk size equal to the total size of the sample), or the intensity of the source itself. Furthermore, in very extended sources, the object's emission can be confused with the atmosphere, requiring the subtraction of far fewer components or other reduction techniques.[33,34]

Figure 6 illustrates the cleaning process in a typical detector's timestream and its power spectrum. The difference between the raw and the cleaned timestreams is noteworthy; the spikes and the baseline are removed, and the noise is significantly reduced, particularly at low frequencies. Meanwhile, in Fig. 7, we compare the median power spectral densities (PSDs) of the raw and cleaned timestreams for each of the active channels of run 1, from a typical beam map observation of long exposure. Here, the low-frequency tail [the contribution of atmosphere drifts and the two-level system noise intrinsic to the KID] is flattened, the frequency spikes above 36 Hz are suppressed, the three highest signals in each channel below 36 Hz are eliminated, and the noise level is generally lower. Despite the cleaning, a low-frequency signal is preserved, at 1.4 Hz plus its harmonics, a remnant of the PTC operation.

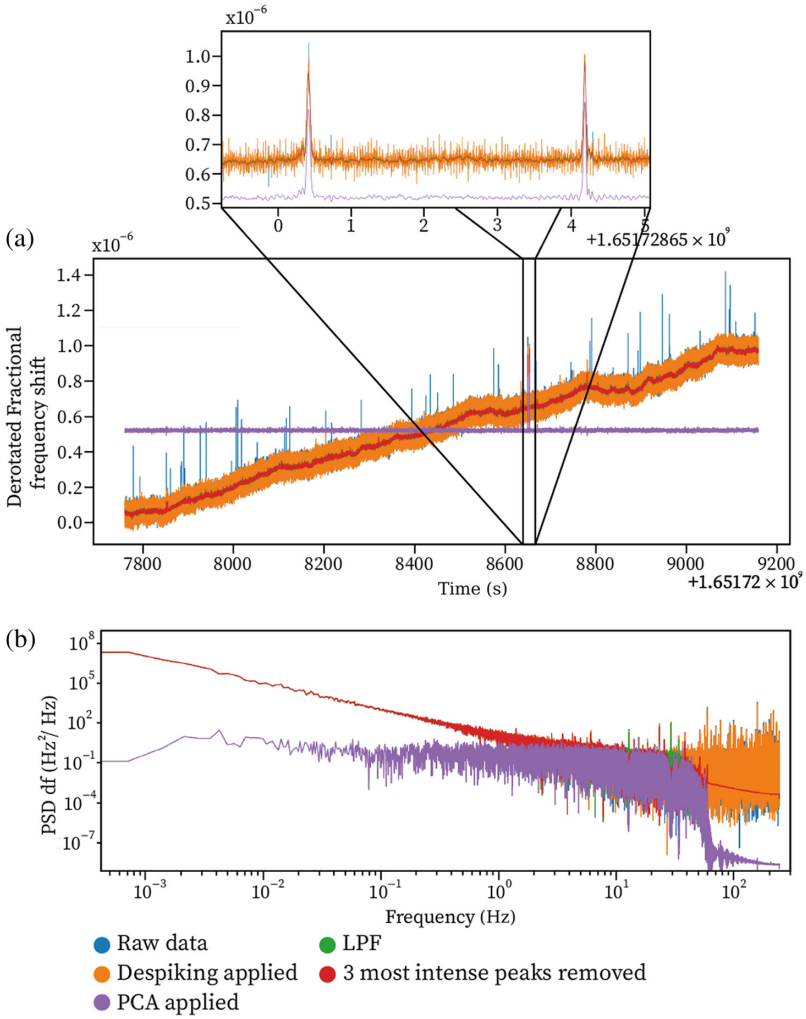

Fig. 6 Evolution of the timestream (a) and its spectrum (b) of a representative detector of the focal plane during the reduction process. To the raw data (blue graph, barely visible), we apply, in the following order: (i) despiking (orange), (ii) sinc-type low-pass filter with a cutoff frequency of 36 Hz (green), (iii) notch filters band-reject in the three most intense peaks below 36 Hz (red), and (iv) removal of principal components using PCA (purple). The zoom-in on the graph above shows the source's response in detail. The signal-to-noise in the cleaned timestream (purple) is visibly higher than the raw data due to the notable noise reduction.

3.3.3 *Post-processing*

We construct the maps per detector by combining the cleaned timestreams with the telescope pointing data. Then, adding the contribution of each detector through inverse–variance weighting, we build the final instrument map.

For the detector beam characterization, the maps presented here are normalized with the amplitude of the source. The atmospheric extinction correction and the flux calibration are out of the scope of this work.

The maps per i'th detector, m_i, are constructed through the discretization of space, linking each point in the timestream with the telescope's position at a given instant. By defining the pixel size in arcseconds, we transform the pointing position of the telescope in a given coordinate system (horizontal or equatorial) to a position on the map in pixels. Every time the telescope passes by a particular pixel, we accumulate the value of the timestream in that position on the map. To create the signal map, we average all the accumulated values at each pixel. In contrast, the coverage map, t_i, is simply the number of times the telescope passes through each pixel divided by the instrument's sampling frequency (~488 Hz).

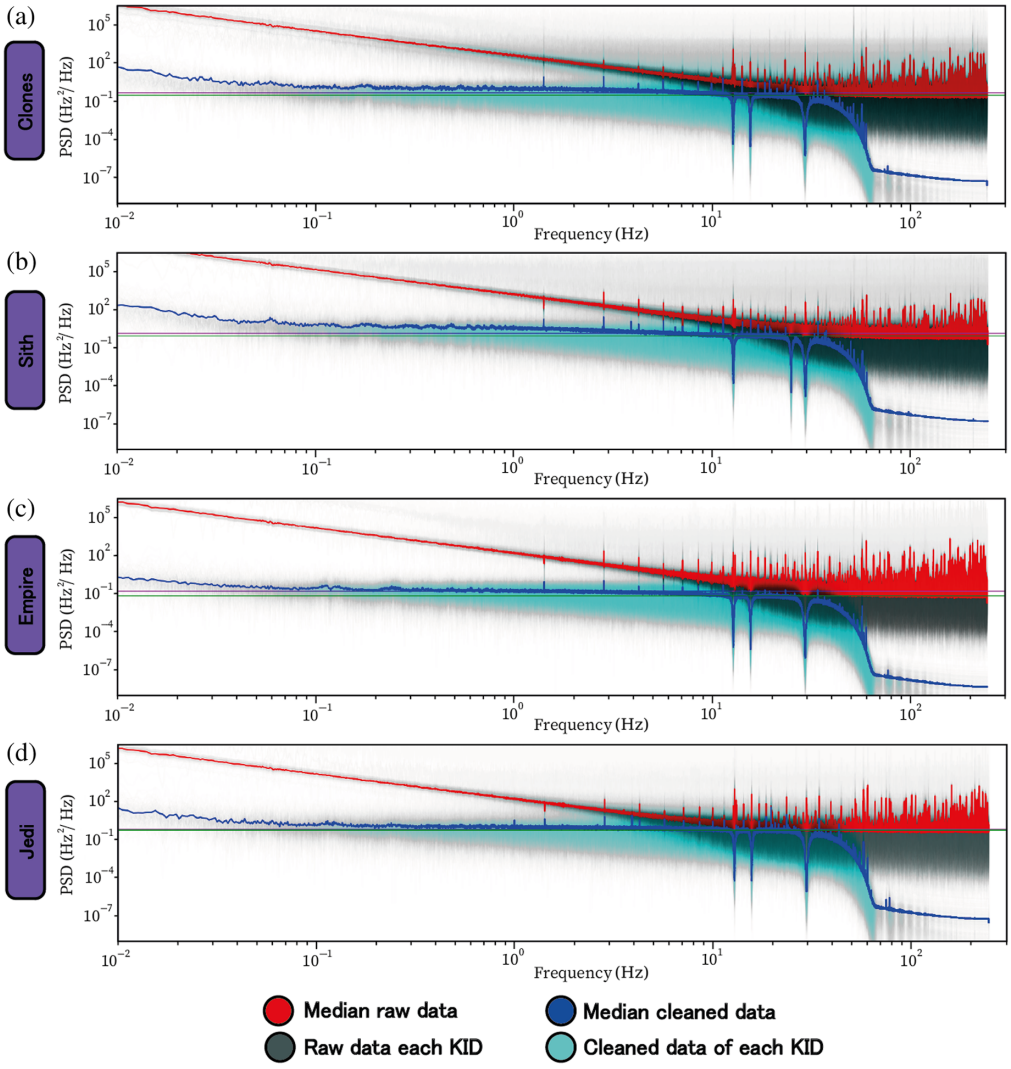

Fig. 7 (a)–(d) Comparison of the PSD of the raw timestreams (black) and their median (red), with the cleaned timestreams (cyan) and their median (blue) of all the detectors of each of the functional channels of run 1. The median cleaned data clearly shows the effect of the MUSpipe processing cleaning tasks: the low-pass filter, the three band-reject filters, and the flattening at low frequencies due to removing the principal components. Furthermore, the average noise level in a flat region of the clean median spectrum (green horizontal line) is lower than that of the raw median spectrum (magenta horizontal line), in array 2 (clones), ranging from 0.42 Hz^2/Hz in the raw data to 0.28 Hz^2/Hz in the cleaned one, from 1.20 to 0.81 Hz^2/Hz in array 3 (sith), 0.14 to 0.06 Hz^2/Hz in array 5 (empire), and from 0.61 to 0.50 Hz^2/Hz in array 6 (jedi).

The detector timestream size must be equal to the pointing telescope file; nonetheless, the sampling rate of MUSCAT is ~10 times that of the LMT, ~50 Hz. So, it is required to linearly interpolate the pointing positions for the time instants defined by the time vector of the timestreams. This interpolation assumes that the speed of the telescope is constant, and this is true in most cases, except in turnarounds for raster scan maps where the data are discarded.

Also, we create a weight map per detector, w_i, multiplying the coverage map by a factor K_i that depends on the noise of the signal map, so that the least noisy detectors weigh more when all their maps are coadded. This K_i is calculated by masking the source in the detector signal map at a radius four times the full width at half maximum (FWHM) of the telescope's diffraction limit, as well as the turnaround areas of the raster map. The factor is calculated as the inverse of the variance of the remaining pixels on the map. We discard all the detectors whose weights are above five times the mean value (detectors with unusually high weights tend to dominate the

construction of the map, i.e., the coadded map ends up reproducing the characteristics of the maps of these detectors; hence, they should be excluded).

The instrument's signal map, M_s, is built by coadding the signal maps of all detectors, m_i, weighting them according to their w_i map, as

$$M_s = \frac{\sum_i^N m_i w_i}{\sum_i^N w_i}, \tag{1}$$

where N is the total number of functional detectors.

The total coverage map, M_t, is obtained by adding the individual coverage maps of each detector as

$$M_t = \sum_i^N t_i. \tag{2}$$

Similarly, the total weight map, M_w, assuming that the noise from each detector is random and independent, is calculated as the sum of all weight maps per detector

$$M_w = \sum_i^N w_i. \tag{3}$$

From the signal M_s and weights M_w maps, we calculate the signal-to-noise map M_{SNR}, as

$$M_{\mathrm{SNR}} = M_s \sqrt{M_w}. \tag{4}$$

If the detector noises are all independent, the histogram of the signal-to-noise map far from the source should have a width close to 1. However, in all the maps reduced by MUSpipe, the width ranges between 1.8 and 2.2, which reveals a noise correlation among the detectors. Following the methodology of Perotto et al.,[12] we get the corrected weight map, $M_{w,\mathrm{corr}}$ as

$$M_{w,\mathrm{corr}} = M_w / w_{\mathrm{SNR}}^2, \tag{5}$$

where w_{SNR} is the histogram width of the signal-to-noise map far from the source. The signal-to-noise map is recalculated according to Eq. (4).

3.4 Detector Positions

By fitting an elliptical Gaussian function to the individual maps per detector, m_i, we obtain the positions, widths, and amplitudes of the point source, revealing the radiation pattern of each detector. Subsequently, averaging the detectors' positions of the observations in Table 1, we obtain their mean positions and their error bars, taking into account the following considerations:

- We correct the pointing offsets (associated with pointing error and the particular conditions of the optics for a given observation, mainly defined by the primary mirror) of each observation, calculating the average distance between the positions of the detectors of a given observation and those of the reference observation 094468, subtracting it from all the detectors.
- We average the detector positions as long as it has been recorded in at least five beam map observations. There are several reasons why we locate the position of a detector in some observations and not in others. Firstly, according to the connectivity criterion, some detectors labeled as "bad" may be so in some and not in others, depending on the atmospheric conditions of the observation and the success of the tuning. In addition, due to the finiteness of the raster scan step, there are some cases where the detectors do not pass through the center of the source. If, in addition, the size of the pixel is small, the uncertainty about the calculated position is high, or in the worst case, it cannot even be located.
- If the detector position is determined in all observations, but the standard deviation is greater than 10 arcsec in any axis, we eliminate the outliers and recalculate the position and its error. Glitches on the maps can lead to false detections in positions far from the real detector, producing a very high dispersion when averaging all positions. Removing the outliers ensures that the remaining points belong to actual detections.

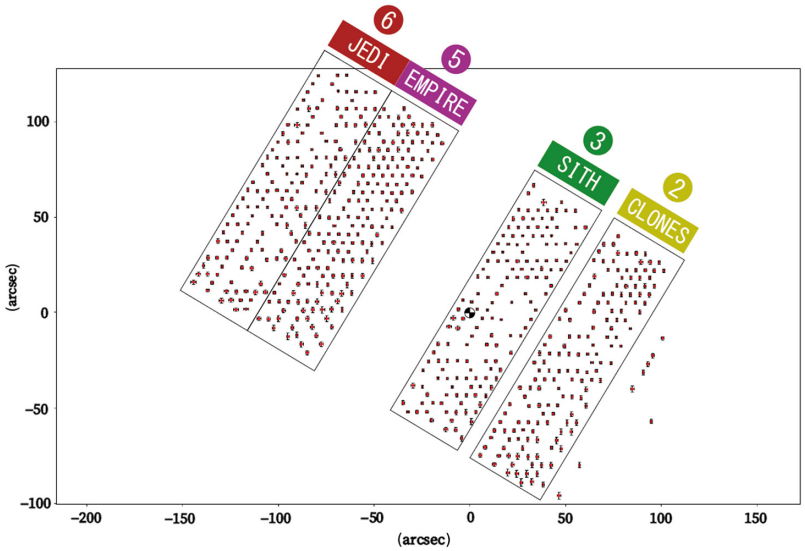

Fig. 8 Positions of the available detectors for run 1 (red dots) grouped by arrays 2, 3, 5, and 6 (from right to left and from bottom to top) in the focal plane with their error bars (black lines), according to the analysis of the beam map observations of Table 1. There is a total of 636 useful detectors. The blank space in the center and far right of the array belongs to the detectors of arrays 4 and 1, respectively, which could not be located due to problems in their readout lines during the observations. The few detectors observed to the right of array 2 are the cross-talk of some resonators of array 1. Their response is preserved as part of array 2, to whose transmission line they are mounted, due to an SNR and position errors similar to those of a typical detector of array 2.

4 Results

4.1 Arrays Yield

Figure 8 shows the average positions of the detectors in the focal plane corresponding to arrays 2, 3, 5, and 6, along with their associated error bars. We clearly distinguish each array's space, with nine columns of 27 detectors each. Numerous empty regions are observed, where the detectors are damaged, malfunctioning, or their resonance frequencies are out of the readout bandwidth (as presented in Tapia et al.,[27] the resonance frequencies in the arrays 5 and 6, which belongs to an older design, are more dispersed than the others, and a significant number of detectors are outside the readout bandwidth). The average on-sky distances between the centers of the adjacent detectors are 5.08 ± 0.27, 5.16 ± 0.36, 5.11 ± 0.22, and 5.11 ± 0.25 arcsec for arrays 2, 3, 5, and 6, respectively; consistent along the focal plane and very close to the design value of 5 arcsec ($1\,f\lambda$).[27]

We obtain the position error histograms of Fig. 9 from the error positions by array. In general, we observe that the position error in the x-axis, or azimuth, persists in all detector arrays, with a mean value of 0.62, 0.62, 0.68, and 0.66 arcsec for arrays 2 (clones), 3 (sith), 5 (empire), and 6 (jedi), respectively.

The position error in the y-axis, or elevation, changes along the focal plane, having a mean value of 1.03, 0.74, 0.99, and 0.84 arcsec for arrays 2, 3, 5, and 6, respectively. The average error in array 3, in the center of the focal plane, is similar in both axes, whereas in arrays 2 and 5, the elevation error is significantly greater. However, in all cases, the error is well below the average center-to-center distance between detectors of ∼5 arcsec.

From the position map in Fig. 8, we count 636 detectors distributed as 165, 151, 181, and 139 in arrays 2, 3, 5, and 6, respectively. This amount represents a yield of 65%, similar to the reported for the six arrays in the laboratory.[27]

4.2 Detectors Beam Shape

Having the detector positions, we get the instrument's signal maps of the beam maps observations of Table 1, shown in the mosaic of Fig. 10. Qualitatively, we see that the beams for all Neptune observations are severely distorted, with multiple sidelobes. In addition, the beam has

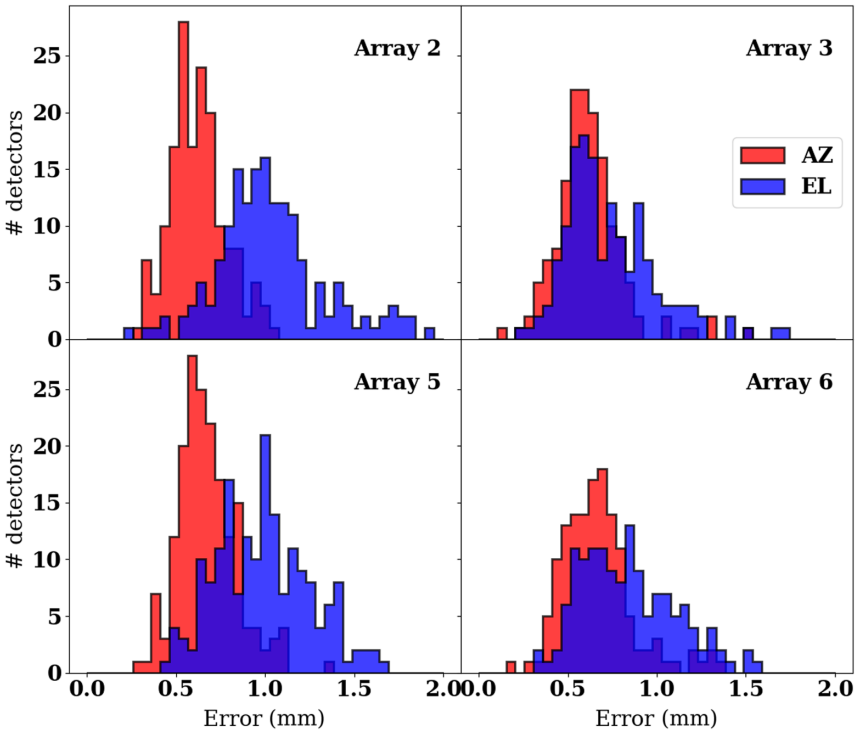

Fig. 9 Histograms of the detector position errors for each MUSCAT array. In all arrays, the errors in azimuth, or *x*-axis (red), have distributions with similar mean values: 0.62 arcsec, 0.62 arcsec, 0.68 arcsec, and 0.66 arcsec for arrays 2, 3, 5, and 6; more than seven times below the average distance between detectors (5 arcsec). On the other hand, the errors in elevation (blue) vary slightly depending on the array: in array 3 (in the center of the focal plane), they are similar to errors in azimuth, 0.74 arcsec; in array 6, the difference is slightly higher, with 0.84 arcsec, being in arrays 2 and 5 where the elevation error is greater, with 1.03 arcsec and 0.99 arcsec, respectively.

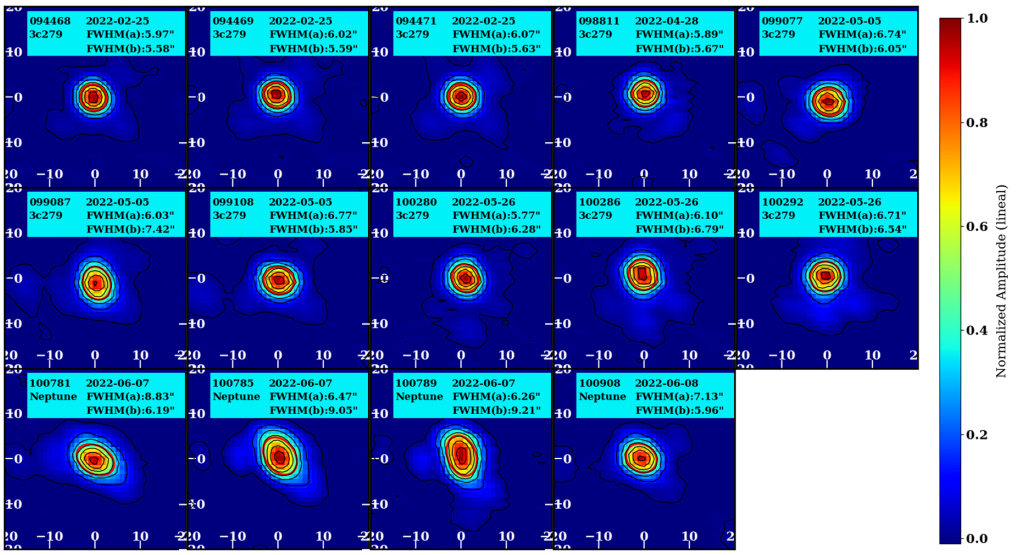

Fig. 10 Mosaic of beam map observations with MUSCAT during run 1, normalized with the amplitude of the source. The first two rows correspond to observations of source 3C279 and the last one to Neptune. The results of the elliptical Gaussian fitting are shown in the upper cyan rectangle, represented in the map by a red ellipse. The rectangle also shows the observation number, date, and source name. All observations of Neptune, along with 099087 and 100292 of 3C279, present distorted beams (broadened and elongated), so they were excluded from the rest of the analysis. The black contours show the seven levels evenly distributed between the maximums and minimums of each map.

Table 2 Major and minor axes width results from the elliptical Gaussian fit of the selected beam map observation of run 1, as well as the mean value and the error estimated as the standard deviation.

ObsNum	Major axis (arcsec)	Minor axis (arcsec)
094468	5.97	5.58
094469	6.02	5.59
094471	6.07	5.63
098811	5.89	5.67
099077	6.74	6.05
099108	6.77	5.85
100280	6.28	5.77
100286	6.79	6.10
Mean	6.32	5.78
Error	0.36	0.19

broadened, revealing that the camera was out of focus and had to be excluded from the beam shape analysis. Moreover, observations 099087 and 100292 of blazar 3C279 are also visibly deformed. The first is elongated, with the major axis exceeding 7 arcsec, and the second is widened, with both axes exceeding 6.5 arcsec in length. These observations are also discarded for the beam analysis.

We average the fit beam FWHM of each of the remaining observations, summarized in Table 2, obtaining a width on the major axis of 6.32 ± 0.36 and 5.78 ± 0.19 arcsec for the minor axis. The average beam has a slight elongation, with an eccentricity of 0.40 and a marginal widening concerning the expected beam defined by the diffraction limit of 5 arcsec.

From the widths obtained from the individual map fits, using only the observations selected in Table 2, we calculate the average widths of the detector beams in the major and minor axes. In Fig. 11, we present the histograms of the resulting widths grouped by detector arrays.

First, we note that in all the arrays, the distributions of both axes have a Gaussian behavior. Furthermore, there is a clear separation between the major and minor axis distributions, suggesting that the vast majority of detectors have visibly elongated beams.

The average widths in the major/minor axes are 6.77/4.97, 6.66/4.91, 6.92/5.03, and 7.02/5.10 arcsec for arrays 2, 3, 5, and 6, respectively. These results show that the beams are slightly more compact in the central array 3 (sith), and as we move away, the beams widen slightly.

To better understand this behavior, we plot the beams of each detector as ellipses with a major/minor axis, centered on their position in the focal plane, assigning a color based on the average length of their axes, as shown in Fig. 12.

Array 3 concentrates many detectors with narrow beams, mainly at the upper and lower ends. Starting from the central region, the beams widen toward the ends, particularly toward arrays 5 and 6, as the histograms indicate. Like array 3, array 2 shows a small group of detectors with narrow beams at the top, with the rest marginally wider. The distribution of the beam widths in array 5 is notable, where the upper part concentrates on the narrower beams and the lower part on the wider ones. In array 6, the distribution is more homogeneous, with a slight gradient of beam widening from the top to the bottom.

Figure 13 shows the heat map of the detector's eccentricity along the focal plane. The groups of narrower beams identified in the heat map of the average widths coincide with those regions where the beams are also more elongated, with an approximate eccentricity of 0.7. So, we observe that the narrowest beams are also the most elongated.

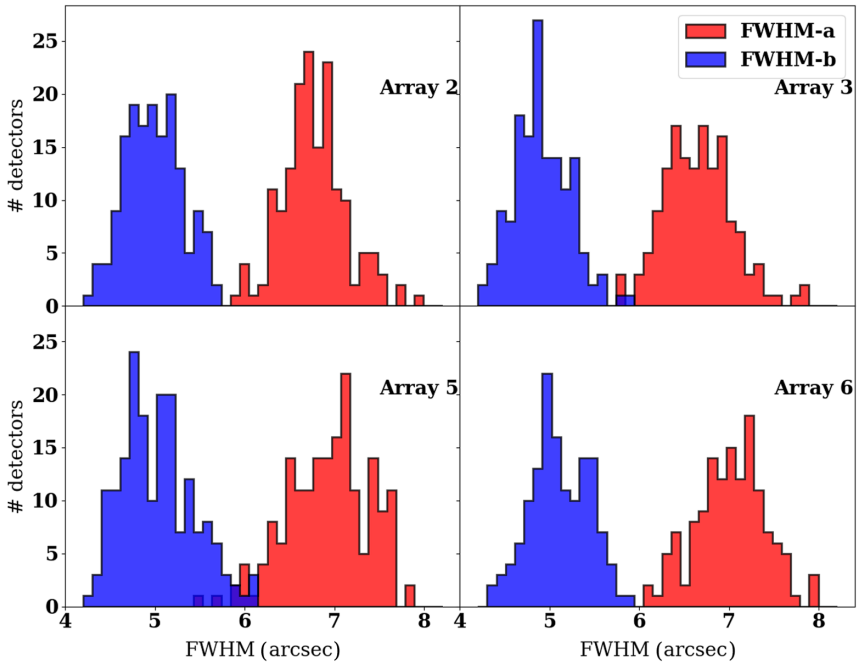

Fig. 11 Histograms of the MUSCAT detectors' beam widths (major and minor axes) grouped by arrays. The well-marked separation between the distributions of the major (red) and minor (blue) axes shows a slight elongation in all beams. Calculating the average values of the distributions, we see that in general, the detectors of array 3 (sith) have the most compact beams, 6.66 arcsec × 4.91 arcsec, widening minimally in the rest of the arrays: 6.77 arcsec × 4.97 arcsec (2), 6.92 arcsec × 5.03 arcsec (5), and 7.02 arcsec × 5.10 arcsec (6).

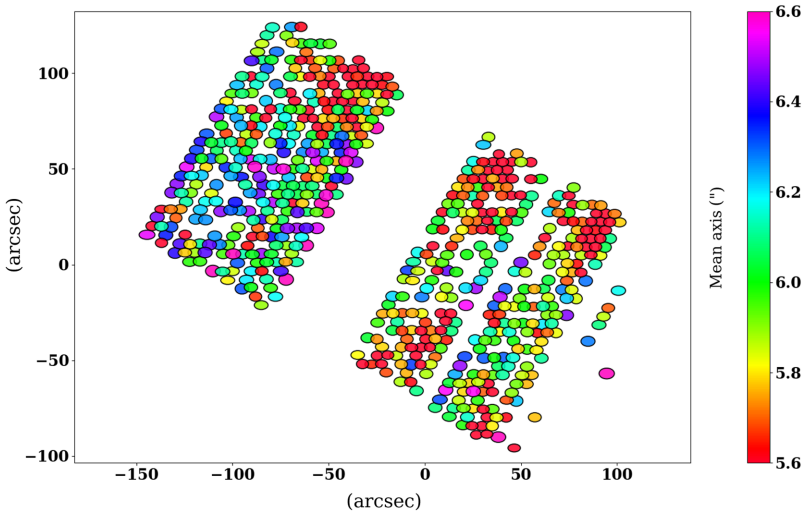

Fig. 12 Heat map of the mean beam widths of the functional detectors of run 1 relative to their position in the focal plane (array 2 to 6, right to left). The detectors of array 3 have the most compact beams, mainly at the top/bottom ends. In array 2, the distribution is homogeneous, with a region at the top of detectors with narrower beams. In array 5, two populations are distinguished, one with compact beams (upper) and others with wide ones (lower), whereas in array 6, the width distribution is more uniform. Each detector is represented by an ellipse whose major and minor axes correspond to the average combination of the selected beam map observations.

The above beam shape distribution does not coincide with the distribution observed in the laboratory, reported in Tapia et al.[27] So, it is unlikely that the pattern observed in the laboratory was due to a tilt in the detector arrays or to some cold optics alignment problem inside the instrument, suggesting instead it was a characteristic of experiment setup: artificial source radiation

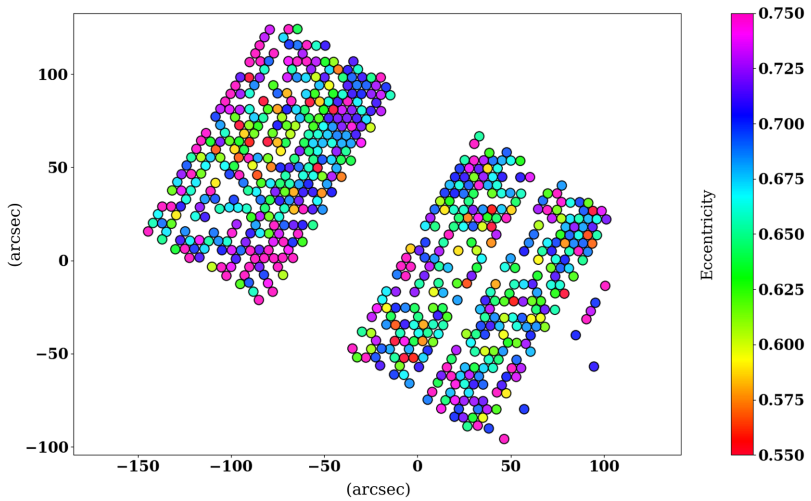

Fig. 13 Heat map of the eccentricities of the MUSCAT focal plane functional detectors, grouped in arrays 2, 3, 5, and 6 (right to left). We observed some spots along the focal plane where the beams are slightly more elongated. However, this distribution generally does not reproduce the pattern observed in the laboratory.[27] A circle with a radius of 2.5 arcsec represents each detector.

pattern, the optical alignment with the instrument, or the properties of the imaging lens mounted on the cryostat window and not to an intrinsic property of the camera.

4.3 MUSCAT Stacked Beam

To study the sidelobes in the MUSCAT-LMT beam, we coadd the normalized maps of the selected beam map observations in Table 2 through inverse-variance weighting, obtaining the maps, in linear and logarithmic scale (in dB), of Figs. 14 and 15, respectively.

The elliptical Gaussian fit results in a width of 6.22 arcsec × 5.80 arcsec, very similar to the mean value calculated previously and reported in Table 2. The structure formed outside the source is of great interest, highlighting the three interconnected spots in the beam's northeast, southeast, and southwest corners. Initially, based on the first observations, in Tapia et al.,[35] we attributed the shape of the sidelobes to the tetrapod that supports the M2 mirror. However, in light

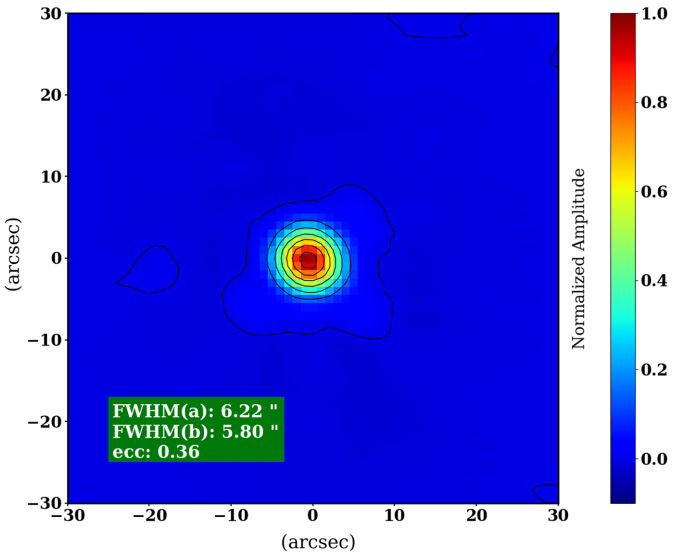

Fig. 14 MUSCAT stacked beam in linear scale, coadding the normalized sources selected in Table 2. The beam has a slightly elongated circular shape, with a width of 6.22 arcsec/5.80 arcsec on the major/minor axes. Some sidelobes are seen in the northeast, southeast, and southwest corners, with an additional spot 20 arcsec west of the beam.

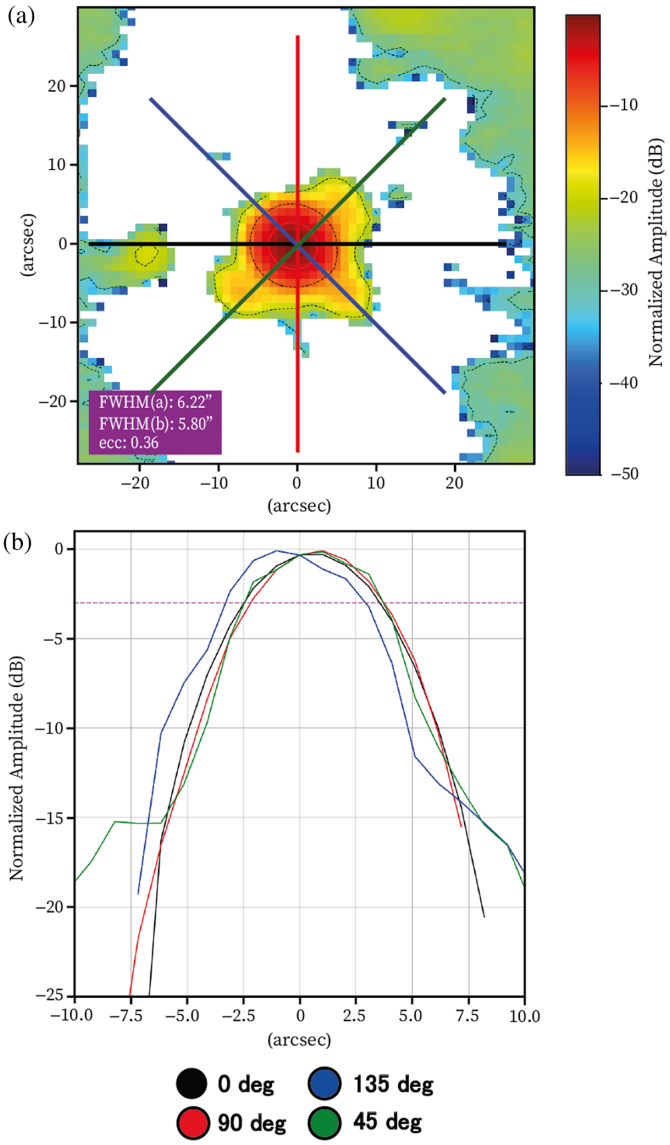

Fig. 15 (a) MUSCAT stacked beam in logarithmic-scale and (b) its profiles at 0 deg (black line), 45 deg (green), 90 deg (red), and 135 deg (blue). The blank region in the left graph shows the negative over-subtraction zone around the source.

of the contribution of the rest of the observations, the weak northwest structure seen in the first maps fades, losing the expected symmetry of the tetrapod.

In some maps, such as observations 098811 and 099077, the sidelobes only reproduce one stacked beam spot, the southeast and southwest, respectively. In addition, in observations 100280 and 100286, taken consecutively on the same night, the sidelobes present an additional spot just south of the beam.

In summary, the main sidelobe structures in the stacked beam are due to the contribution of the consecutive observations of February 25 and May 26, whereas the other observations contribute to one or the other of the structures. More observations are required to clearly delineate the sidelobes intrinsic to the MUSCAT-LMT optical system without the particularities of a given observation night dominating.

To analyze the sidelobe amplitudes relative to the source maximum, using the logarithmic-scale map at the top of Fig. 15, we plot the slices at 0, 45, 90, and 135 deg, presented in the bottom graph of Fig. 15.

The slices at 0 and 90 deg cross the portions of the beam where the effect of the sidelobes is minimal (in a radius less than 10 arcsec, neglecting the impact of the spot 20 arcsec to the left of

the beam). The profiles of both curves are similar, with the horizontal slightly wider due to the slight elongation of the beam. Referencing the slice at 0 deg, the curve crosses −20 dB at 6.4 arcsec left of center and 8.1 arcsec to the right. At these radial positions, the vertical profile has a value of −17.8 dB at 6.4 arcsec to the left of the center and an indeterminate (negative) value at 8.1 arcsec to the right.

As for the slice at 45 deg, which passes through two of the most prominent sidelobe structures, at 6.4 arcsec to the left of the center, the intensity of the profile is −15.3 dB and at 8.1 arcsec to the right of −15.2 dB. That is, in both cases, the lobe's intensity is ∼5 dB greater than the intensity of a non-lobe area in the same radial distance, where the impact of the sidelobes is minimal. In other words, the amplitudes of these sidelobes are equivalent to ∼3% about the center of the source.

Finally, the slice at 135 deg, which passes through the remaining southeast spot, has an amplitude of −12.5 dB at 6.4 arcsec to the left of the beam and −15.2 dB to the right, where it is located the sidelobe. In these radial positions, and because the slice is aligned with the major axis of the beam, the left point is more intense as it is still positioned in part of the main beam. At the same time, the right region, which is above the sidelobe, has an intensity similar to the other spots, ∼3% of the source amplitude.

Two more characteristics stand out in the MUSCAT-LMT stacked beam. The first is the spot 20 arcsec west of the center of the beam, with a maximum amplitude of ~ -22 dB (less than 1% relative to the main beam amplitude). The second, more relevant is the negative region of over-subtraction (the blank region in Fig. 15), which surrounds the source in a radius greater than 20 arcsec, originating from the PCA cleaning.

5 Conclusions

During the first MUSCAT commissioning season at the LMT, observing the bright point-like sources 3C279 and Neptune, we obtained the camera's yield and characterized the detector beams of arrays 2, 3, 5, and 6 of the focal plane. From the 14 beam map observations, we obtained the average positions of the available detectors in the focal plane. The average center-to-center distance between detectors is just over 5 arcsec, similar to the design distance of $1\,f\lambda$, equivalent to the size of a beam at the diffraction limit.

Of the four readable arrays, we found a total of 636 functional detectors, equivalent to 65% of the fabricated detectors. These are distributed as 165, 151, 181, and 139 in arrays 2, 3, 5, and 6, respectively. Except for array 6, whose yield is meager, the rest of the arrays present values similar to those obtained in the laboratory, as reported in Tapia et al..[27] The slight differences are due to multiple factors: the oxidation developed in the aluminum layer of the detectors among the cooling downs of both measurements, the selection of the local oscillator frequency and thus the range of readout frequencies, which mainly affect arrays 5 and 6 whose resonant frequencies exceed the readout bandwidth. Assuming that the yield is preserved in arrays 1 and 4, after repairs to the readout lines, we expect a total of ∼950 detectors within the six arrays.

An important fraction of the discarded detectors, ∼5%, is due to detectors whose resonance frequencies are out of the readout bandwidth, mainly in arrays 5 and 6. The number of unreadable detectors decreased considerably with the reduction of the average distance between resonators in arrays 1 to 4.[27]

Moreover, ∼10% of the detectors are excluded for presenting collisions at their resonance frequencies. The resonator collision problem could be addressed from several fronts. Improving the manufacturing process reduces errors in the dimensions of the deposited tracks enhances the uniformity and controls the dispersion of the resonators. On the other hand, there are some corrective techniques to adjust the resonance frequency of the colliding detectors through a second lithography process that modifies the resonator capacitance, reporting yields of up to 97% for arrays with more than 2000 resonators.[36]

However, the most significant impact on MUSCAT yield is the loss of complete arrays due to failures in the readout lines. Although the main advantage of KIDs over other forms of detection, such as TES, is the significant readout complexity reduction, using a single transmission line, failures in this line also affect all detectors mounted to it. In future repairs and updates, the proper

functioning of the transmission lines must be guaranteed, reducing the risk points through more reliable cryogenic cables resistant to thermal stress, such as crimped coaxial cables.

Despite the initial setup, the beam in some of the observations shows visible broadening and distortions, which is why, of the 14 observations, we only use eight to characterize the beams. Thus, we estimate the average FWHM of 6.32 arcsec $\pm$ 0.36 arcsec $\times$ 5.78 arcsec $\pm$ 0.19 arcsec, slightly elongated with an eccentricity of 0.40, and marginal broadening concerning the expected beam at the diffraction limit of 5 arcsec.

The broadening and slight elongation of the beam arise from multiple factors. The M1 mirror roughness may not be optimal, considering that the telescope was halted for almost two years due to the COVID-19 health emergency, without the periodic corrections applied to the antenna surface before the observation season. Also, although with less impact, the tetrapod supporting the M2 mirror reduces the antenna's effective diameter, so the expected beam at the diffraction limit is slightly wider. In addition, we must add the minimum deviations in the optical alignment between the telescope and the camera, as well as the instrument's response: alignment of the cold optics, feedhorns, and detectors.

Also, we identify regions where the beams are slightly narrower and elongated in the focal plane. However, the pattern observed in the laboratory measurements of Tapia et al.[27] is not reproduced, where the beams gradually narrow and become more elongated from the top right corner (top array 1) to the bottom left corner (bottom array 6). Our results suggest that the distribution observed in the laboratory is an artifact imposed by the experiment setup, the artificial source, or the optical alignment, and not an inherent property of the instrument's focal plane or the internal optics.

We also observe that the detector beam widths broaden subtly from the center (array 3) to the ends of the focal plane. The information from the unavailable arrays 1 and 4 will help to discern whether it is a general trend in the focal plane or a local property of each array.

Finally, the MUSCAT beam's sidelobes are predominantly formed by three spots in the northeast, southeast, and southwest corners, with a maximum intensity of approximately 3% of the main beam amplitude. We also found a spot 20 arcsec west of the source with an amplitude of $\sim$1% of the main beam. However, further observations are required to clarify whether these sidelobes correspond to an intrinsic property of the MUSCAT-LMT system and are not dominated by the particular conditions of the few nights of observations performed during run 1.

Disclosures

No conflicts of interest to declare.

Code and Data Availability

We provide the code to replicate the results presented here in the GitHub repository: https://github.com/MarcialX/MUSCAT-JATIS-2024-paper.git.

The FITS maps required for the code above are available here: https://drive.google.com/drive/folders/1o53B-vBzPF800JAYTVq-MSAhNESiLXIf?usp=sharing.

The raw data from which the FITS maps were generated is not public yet.

Acknowledgments

We acknowledge Research Councils United Kingdom and Consejo Nacional de Humanidades, Ciencias y Tecnologías (CONAHCYT) through the Newton Fund project ST/P002803/1, CONAHCYT for supporting the fellowship for the instrument scientist (Grant no. 053), Chase Research Cryogenics for the development of the sub-Kelvin coolers and to XILINX Inc. for the donation of the FPGAs used for the ROACH2 boards.

We especially thank the LMT team for the invaluable support, from installing the camera on the telescope to its continued operation.

In Tapia et al.,[35] an SPIE Proceeding presented at the Millimeter, Submillimeter, and Far-Infrared Detectors and Instrumentation for Astronomy XI conference, we presented the preliminary results of the beam characterization of the MUSCAT focal plane detectors based on the first week of observations in the LMT. In this article, we extend and deepen the analysis using all the observations from the 2022 campaign under varied atmospheric conditions.

References

1. M. G. Hauser and E. Dwek, "The cosmic infrared background: measurements and implications," *Annu. Rev. Astron. Astrophys.* **39**, 249–307 (2001).
2. P. Day et al., "A broadband superconducting detector suitable for use in large arrays," *Nature* **425**, 817–821 (2003).
3. K. Irwin and G. Hilton, *Transition-Edge Sensors*, pp. 63–150, Springer Berlin Heidelberg, Berlin, Heidelberg (2005).
4. M. H. Abitbol et al., *CMB-S4 Technology Book*, 1st ed., arXiv:1706.02464 (2017).
5. I. Lowe et al., "The Balloon-borne Large Aperture Submillimeter Telescope Observatory," *Proc. SPIE* **11445**, 114457A (2020).
6. G. L. Pilbratt et al., "Herschel Space Observatory: an ESA facility for far-infrared and submillimetre astronomy," *Astron. Astrophys.* **518**, L1 (2010).
7. W. S. Holland et al., "SCUBA: a submillimeter camera operating on the James Clerk Maxwell Telescope," *Proc. SPIE* **3357**, 305–318 (1998).
8. D. H. Hughes et al., "High-redshift star formation in the Hubble Deep Field revealed by a submillimetre-wavelength survey," *Nature* **394**, 241–247 (1998).
9. A. J. Barger et al., "Submillimetre-wavelength detection of dusty star-forming galaxies at high redshift," *Nature* **394**, 248–251 (1998).
10. J. T. Dempsey et al., "SCUBA-2: on-sky calibration using submillimetre standard sources," *Mon. Not. R. Astron. Soc.* **430**, 2534–2544 (2013).
11. A. Catalano et al., "Performance and calibration of the NIKA camera at the IRAM 30 m telescope," *Astron. Astrophys.* **569**, A9 (2014).
12. L. Perotto et al., "Calibration and performance of the NIKA2 camera at the IRAM 30-m Telescope," *Astron. Astrophys.* **637**, A71 (2020).
13. D. H. Hughes et al., "The Large Millimeter Telescope: current status and telescope performance," *Proc. SPIE* **12182**, 1218213 (2022).
14. G. W. Wilson et al., "The AzTEC mm-wavelength camera," *Mon. Not. R. Astron. Soc.* **386**, 807–818 (2008).
15. G. W. Wilson et al., "The TolTEC camera: an overview of the instrument and in-lab testing results," *Proc. SPIE* **11453**, 1145302 (2020).
16. T. L. R. Brien et al., "MUSCAT: the Mexico-UK Sub-Millimetre Camera for AsTronomy," *Proc. SPIE* **10708**, 107080M (2018).
17. T. L. R. Brien et al., "Pre-deployment verification and predicted mapping speed of MUSCAT," *Proc. SPIE* **11453**, 1145303 (2020).
18. S. Doyle, "Lumped element kinetic inductance detectors," PhD thesis, Cardiff University, Cardiff, UK (2008).
19. V. Gómez-Rivera et al., "Design and characterization of the MUSCAT detectors," *Proc. SPIE* **11453**, 114531Q (2020).
20. M. Becerril-Tapia, "Readout and characterization system for kinetic inductance detectors (KID) of the MUSCAT project," Master thesis, Instituto Nacional de Astrofísica, Óptica y Electrónica, Santa María Tonantzintla, Puebla, México (2019).
21. S. Gordon et al., "An open source, FPGA-based LEKID readout for blast-TNG: pre-flight results," *J. Astron. Instrum.* **5**(4), 1641003 (2016).
22. S. Rowe et al., "The MUSCAT readout electronics backend: design and pre-deployment performance," *J. Low Temp. Phys.* **211**, 289–301 (2023).
23. T. L. R. Brien et al., "A continuous 100-mK helium-light cooling system for MUSCAT on the LMT," *J. Low Temp. Phys.* **193**, 805–812 (2018).
24. T. L. R. Brien et al., "The Mexico UK Sub-mm CAMERA for AsTronomy (MUSCAT) on-sky commissioning: performance of the cryogenic systems," *Proc. SPIE* **12190**, 1219018 (2022).
25. C. Dragone, "Offset multireflector antennas with perfect pattern symmetry and polarization discrimination," *Bell Syst. Tech. J.* **57**(7), 2663–2684 (1978).
26. H. Tran et al., "Comparison of the crossed and the Gregorian Mizuguchi-Dragone for wide-field millimeter-wave astronomy," *Appl. Opt.* **47**, 103–109 (2008).
27. M. Tapia et al., "MUSCAT focal plane verification," *Proc. SPIE* **11453**, 1145309 (2020).
28. G. M. Klemencic et al., "A continuous dry 300 mK cooler for THz sensing applications," *Rev. Sci Instrum.* **87**, 045107 (2016).
29. M. Gurkwell, "Submillimeter Calibrator List, SMA Observer Center," http://sma1.sma.hawaii.edu/callist/callist.html (2024).
30. J.-Y. Kim et al., "Event horizon telescope imaging of the archetypal blazar 3c 279 at an extreme 20 micro-arcsecond resolution," *Astron. Astrophys.* **640**, A69 (2020).
31. M. Becerril-Tapia, "Muspipe," https://github.com/MarcialX/MUSpipe (2023).

32. I. Batyrshin et al., *Moving Approximation Transform and Local Trend Associations in Time Series Data Bases*, pp. 55–83, Springer Berlin Heidelberg, Berlin, Heidelberg (2007).
33. C. E. Romero et al., "Inferences from surface brightness fluctuations of Zwicky 3146 via the Sunyaev-Zel-Dovich effect and X-ray observations," *Astrophys. J.* **951**, 41 (2023).
34. E. Chapin et al., "SMURF—the Sub-Millimetre User Reduction Facility," Starlink User Note **258** (2013).
35. M. Tapia et al., "The Mexico UK Sub-mm Camera for Astronomy (MUSCAT) on-sky commissioning: focal plane performance," *Proc. SPIE* **12190**, 1219017 (2022).
36. S. Shu et al., "Understanding and minimizing resonance frequency deviations on a 4-in. kilo-pixel kinetic inductance detector array," *Appl. Phys. Lett.* **119**, 092601 (2021).

Marcial Becerril Tapia holds a PhD in astrophysics, specializing in astronomical instrumentation, from Instituto Nacional de Astrofísica, Óptica y Electrónica (INAOE) in Mexico. His work focuses on developing, analyzing, and characterizing Kinetic Inductance Detectors for large-format cameras, such as MUSCAT and TolTEC at the LMT, and the Simons Observatory in Chile.

Biographies of the other authors are not available.